Volume 9
Number 32
28 August 2021
Pages 10141–10506

Journal of Materials Chemistry C

Materials for optical, magnetic and electronic devices

rsc.li/materials-c

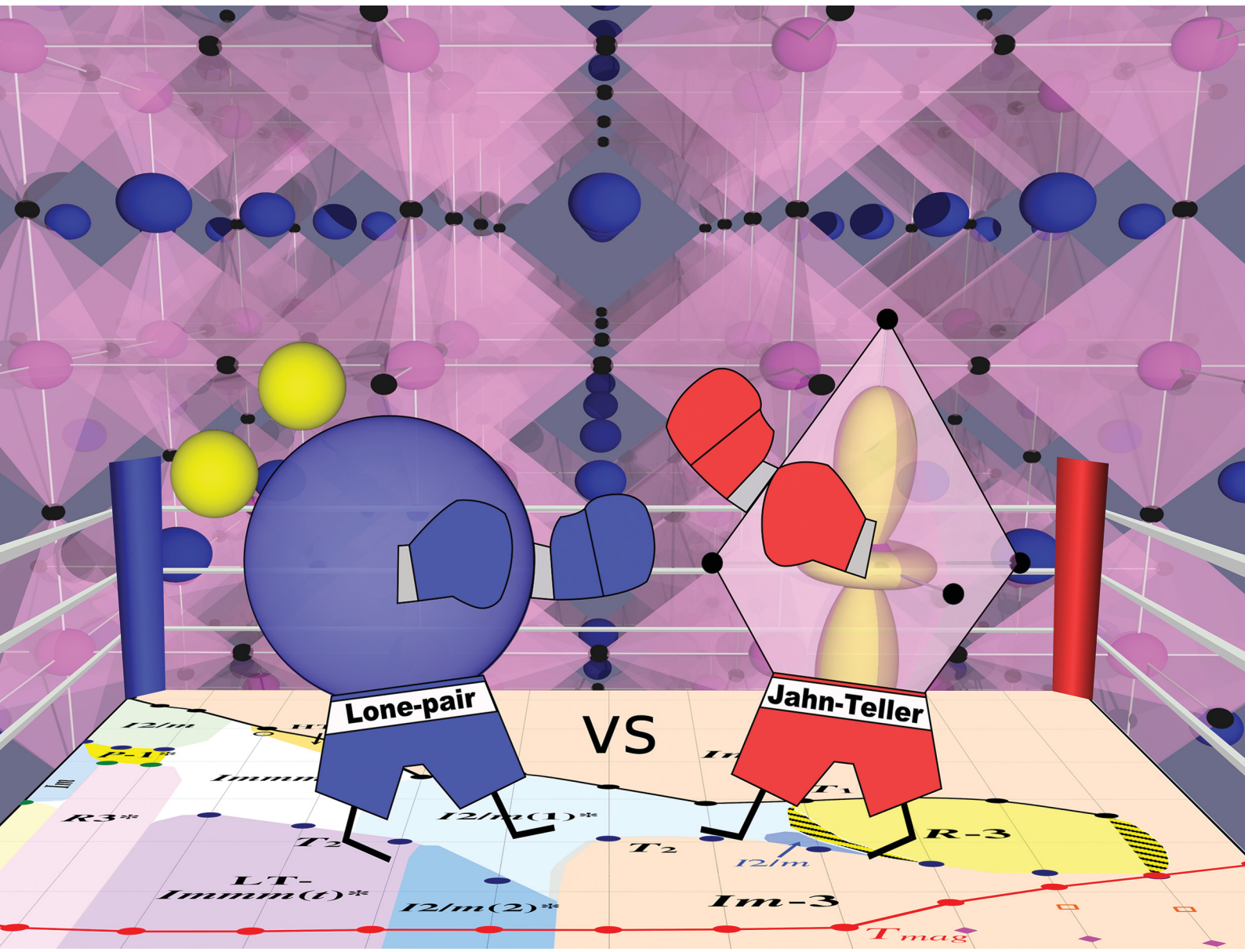

ISSN 2050-7526

ROYAL SOCIETY OF CHEMISTRY

PAPER

Alexei A. Belik *et al.*

A plethora of structural transitions, distortions and modulations in Cu-doped $BiMn_7O_{12}$ quadruple perovskites

Journal of Materials Chemistry C

ROYAL SOCIETY OF CHEMISTRY

PAPER

View Article Online
View Journal | View Issue

Cite this: J. Mater. Chem. C, 2021, 9, 10232

A plethora of structural transitions, distortions and modulations in Cu-doped $BiMn_7O_{12}$ quadruple perovskites†

Alexei A. Belik, *[a] Yoshitaka Matsushita, [b] Masahiko Tanaka,[b] Roger D. Johnson[c] and Dmitry D. Khalyavin [d]

The presence of strongly competing electronic instabilities in a crystalline material can produce fascinating structural phenomena. For example, the A-site-ordered quadruple perovskite $BiMn_7O_{12}$ hosts both active polar instabilities of the Bi^{3+} lone pair electrons and Jahn–Teller instabilities of Mn^{3+} cations that drive the following sequence of phase transformations on cooling, *Im*-3 > *I*2/*m* > *Im* > *P*1, corresponding to orbital ordering and polar distortions. Carrier doping by Cu^{2+} tunes the two instabilities in $BiCu_xMn_{7-x}O_{12}$ solid solutions and significantly complicates the system behavior. The x = 0.05 and 0.1 members show the following sequence of phase transformations on cooling, *Im*-3 > *I*2/*m* > *R*-1(αβγ)0 > *R*3(00γ)*t*, and are examples of materials with the electric dipole helicoidal texture in the ground state and a dipole density wave structure in the intermediate *R*-1(αβγ)0 phase (*Science* 2020, 369, 680–684). Here, the detailed behavior of the $BiCu_xMn_{7-x}O_{12}$ solid solutions with x = 0.2–0.8 was investigated by laboratory X-ray, synchrotron X-ray, and neutron powder diffraction between 5 K and 620 K, and differential scanning calorimetry measurements. Nearly every composition (with a step Δx = 0.1) has a unique behavior when considering both the sequence of phase transitions and the presence of incommensurate superstructure reflections. The sequence *Im*-3 > HT-*Immm*(*t*)* > *Immm** > LT-*Immm*(*t*)* is realized for x = 0.2 and 0.3 (where *t* denotes pseudo-tetragonal), *Im*-3 > *I*2/*m** > *Immm*(*t*)* – for x = 0.4, *Im*-3 > *I*2/*m** > *I*2/*m** – for x = 0.5, *Im*-3 > *I*2/*m** > *Im*-3 – for x = 0.6 and 0.7, and *Im*-3 > *R*-3 > *I*2/*m* > *Im*-3 – for x = 0.8, where asterisks denote the presence of additional incommensurate reflections. Re-entrance of the high-temperature cubic phase was observed at low temperatures for x = 0.6–0.8 suggesting strong competition between the different electronic instabilities. The re-entrant cubic phases have nearly zero thermal expansion.

Received 21st May 2021,
Accepted 7th July 2021

DOI: 10.1039/d1tc02344f

rsc.li/materials-c

1. Introduction

Perovskite-structure (formally trivalent) manganites have surprisingly versatile chemical compositions varying from $R^{3+}MnO_3$ (R = Bi, La-Lu and Y)[1] to $R^{3+}_{1-x}Mn_xMnO_3$ (x is from 0 up to 0.4 depending on the size of R^{3+} cation)[2] to $R^{3+}Mn_3O_6$ (R = Gd–Tm and Y)[3] and finally to $R^{3+}Mn_7O_{12}$ (R = Bi, La-Er and Y).[4–21] Even without any doping they show a broad range of interesting chemical and physical properties originating from an interplay between spin and orbital degrees of freedom, such as one of the largest spin-induced ferroelectric polarization for multiferroic materials of type II[22] and good catalytic activity.[23]

Aliovalent doping introduces a new variable: charge degrees of freedom. This produces more complex phenomena, such as a wider variety of different ground states (including charge- and orbital-ordered insulating antiferromagnets and related stripe structures, ferromagnetic metals, and spin-glass states) and colossal magnetoresistance coupled with phase separation. Doped $R^{3+}_{1-x}A^{2+}_xMnO_3$ perovskites were used as model systems to develop concepts of small polarons, electron–phonon and Jahn–Teller couplings, and double exchange.

In the case of R = Bi a new variable appears: polar instabilities of the Bi^{3+} lone pair electrons. The simple $BiMnO_3$ perovskite was a controversial compound for many years, but experimental[24] and theoretical[25] studies have now established that bulk $BiMnO_3$ crystallizes in a centrosymmetric space group with antipolar

[a] International Center for Materials Nanoarchitectonics (WPI-MANA), National Institute for Materials Science (NIMS), Namiki 1-1, Tsukuba, Ibaraki 305-0044, Japan. E-mail: Alexei.Belik@nims.go.jp
[b] Material Analysis Station, National Institute for Materials Science (NIMS), Sengen 1-2-1, Tsukuba, Ibaraki 305-0047, Japan
[c] Department of Physics and Astronomy, University College London, Gower Street, London, WC1E 6BT, UK
[d] ISIS Facility, Rutherford Appleton Laboratory, Chilton, Didcot, OX11 0QX, UK

† Electronic supplementary information (ESI) available. See DOI: 10.1039/d1tc02344f

displacements of Bi^{3+} cations. On the other hand, A-site-ordered quadruple perovskite $BiMn_7O_{12}$ shows two low symmetry polar phases[12,13] and the following sequence of phase transformations on cooling, *Im*-3 > *I*2/*m* > *Im* > *P*1,[20] where all phases are commensurate. Remarkably, large incommensurate modulations of the structure appear through aliovalent doping by Cu^{2+} in $BiCu_xMn_{7-x}O_{12}$ solid solutions at small x values of 0.05 and 0.1.[26] These compositions exhibit the following sequence of phase transformations on cooling, *Im*-3 > *I*2/*m* > *R*-1(αβγ)0 > *R*3(00γ)*t*, and are the first example of materials with an electric dipole helicoidal texture in the ground state.[26] Moreover, they show a dipole density wave structure in the intermediate *R*-1(αβγ)0 phase.[26]

At high enough doping levels ($x \geq 1.2$), $BiCu_xMn_{7-x}O_{12}$ solid solutions adopt the cubic *Im*-3 structure at all temperatures.[27] At slightly smaller doping levels ($0.9 \leq x \leq 1.1$),[27] where the average oxidation state of B-site manganese is about +3.25, a charge-ordered and orbital-ordered structure at the B sites is first realized, $BiCu^{2+}Mn_2{}^{3+}(Mn^{3+}{}_3Mn^{4+})O_{12}$ – the same structure found in $A^{2+}Mn_7O_{12}$ (= $A^{2+}Mn^{3+}{}_3(Mn^{3+}{}_3Mn^{4+})O_{12}$) perovskites.[28] However, this charge and orbital order in $BiCuMn_6O_{12}$ are stable in a limited temperature range of 300 to 130 K. Below 130 K the charge and orbital orders collapse and the cubic *Im*-3 phase is reentered.[27]

The structural behavior of $BiCu_xMn_{7-x}O_{12}$ solid solutions is remarkable and unique. In this work, we have established the detailed structural properties of $BiCu_xMn_{7-x}O_{12}$ solid solutions in the composition range of $0.2 \leq x \leq 0.8$. We found that almost every composition (with a step $\Delta x = 0.1$) has unique behavior when considering both phase transition sequences and incommensurately modulated superstructure reflections. A *Im*-3 > HT-*Immm*(*t*)* > *Immm** > LT-*Immm*(*t*)* sequence is realized for $x = 0.2$ and 0.3 (where *t* denotes pseudo-tetragonal, and asterisks denote the presence of additional incommensurate reflections), *Im*-3 > *I*2/*m** > *Immm*(*t*)* – for $x = 0.4$, *Im*-3 > *I*2/*m*(1)* > *I*2/*m*(2)* – for $x = 0.5$ (where 1 and 2 distinguish different phases with the same symmetry), *Im*-3 > *I*2/*m** > *Im*-3 – for $x = 0.6$ and 0.7, and *Im*-3 > *R*-3 > *I*2/*m* > *Im*-3 – for $x = 0.8$. A complete composition–temperature phase diagram of $BiCu_xMn_{7-x}O_{12}$ solid solutions was constructed.

2. Experimental part

2.1. Sample preparation

$BiCu_xMn_{7-x}O_{12}$ samples with $x = 0.2$–0.8 and a step of 0.1 were prepared from stoichiometric mixtures of CuO (99.99%), Bi_2O_3 (99.9999%), Mn_2O_3, and $MnO_{1.839}$. $MnO_{1.839}$ is a commercial chemical ('MnO_2' from Alfa Aesar, 99.997%), whose oxygen content was determined to be $MnO_{1.839}$ from the weight loss after heating in air at 923 K for 24 h ($MnO_{1.839}$ was a mixture of Mn_2O_3 and MnO_2 by X-ray powder diffraction). Single-phase Mn_2O_3 was prepared from 'MnO_2' (99.997%) by heating in air at 923 K for 24 h. The mixtures were placed in Au capsules and treated at 6 GPa in a belt-type high-pressure apparatus at about 1370 K for 90 min (heating time to the desired temperature was 10 min). After the heat treatment, the samples were quenched to room temperature, and the pressure was slowly released. The samples were black dense pellets.

2.2. X-ray and neutron powder diffraction

Laboratory X-ray powder diffraction (XRPD) data were collected at room temperature using a RIGAKU MiniFlex600 diffractometer using Cu Kα radiation (2θ range of 10–80°, a step width of 0.02°, and a counting speed of 1° min^{-1}). Some of the $BiCu_xMn_{7-x}O_{12}$ samples contained trace amounts of $Bi_2O_2CO_3$ impurity. Low-temperature (LT) (from 10 K to 300 K) and high-temperature (HT) (from 298 K to 620 K) laboratory XRPD data were collected on a RIGAKU SmartLab using Cu $K\alpha_1$ radiation (45 kV, 200 mA; a 2θ range of 10–110°, a step width of 0.02°, and a scan speed of 2–4° min^{-1}) with a cryostat system and a furnace attachment. XRPD patterns were analyzed and lattice parameters were obtained by the Rietveld method using *RIETAN-2000*.[29] In the LT XRPD experiments, powder samples were fixed with Apiezon-N grease. The surface roughness of the grease/sample mixtures and its evolution with temperature under high vacuum conditions resulted in a larger dispersion of the lattice parameters determined by LT XRPD compared to the lattice parameters determined by HT XRPD.

Synchrotron XRPD data were measured (1) between 110 K and 520 K on a large Debye–Scherrer camera at the undulator beamline BL15XU of SPring-8,[30,31] where the intensity data were collected between 2° and 60.23° at 0.003° intervals in 2θ, and the incident beam was monochromatized at $\lambda = 0.65298$ Å, and (2) between 100 K and 460 K on the beamline BL02B2 of SPring-8,[32] where the intensity data were collected between 2.08° and 78.22° at 0.006° intervals in 2θ, and the incident beam was monochromatized at $\lambda = 0.420138$ Å. The samples were put into Lindemann glass capillaries (inner diameter: 0.1 mm), which were rotated during measurements. Synchrotron XRPD data were analyzed by the Rietveld method using the *RIETAN-2000* program.[29] Sample cooling was performed in air by cold N_2 gas flow; therefore, ice sometimes accumulated on capillaries and produced additional artifact reflections on data collected on BL15XU; those ice reflections could be easily identified in the Rietveld fitting.

Neutron powder diffraction data for $BiCu_{0.5}Mn_{6.5}O_{12}$ were measured at the ISIS pulsed neutron and muon facility of the Rutherford Appleton Laboratory (UK) on the WISH diffractometer located at the second target station.[33] The sample (~1.7 g) was loaded into a cylindrical 6 mm diameter vanadium can and measured from 1.5 K up to 400 K on heating. Rietveld refinements of the crystal structures were performed using the FullProf program[34] against the data measured in detector banks at average 2θ values of 58°, 90°, 122°, and 154°, each covering 32° of the scattering plane.

2.3. Thermal properties

Differential scanning calorimetry (DSC) curves of powder samples (and pellets in a few cases) were recorded on a Mettler Toledo DSC1 STAR^e system at heating/cooling rates of 10 K min^{-1} between 130 K and maximum 650 K in Al capsules.

Three runs were performed to check and confirm very good reproducibility.

3. Results and discussion

3.1. $BiCu_xMn_{7-x}O_{12}$ solid solutions with x = 0.2 and 0.3

DSC measurements (Fig. 1a) of $BiCu_{0.2}Mn_{6.8}O_{12}$ showed the presence of a broad peak on heating, which was centered at $T_1 \approx 500$ K, with tails on both sides from the maximum. In the case of $BiCu_{0.3}Mn_{6.7}O_{12}$, the DSC peak was significantly broader on heating with $T_1 \approx 440$ K (Fig. 1b), and no DSC anomalies were detected on cooling. No DSC anomalies were detected below 300 K in both samples (Fig. S1, ESI†).

Laboratory and synchrotron (Fig. 2) XRPD measurements showed that above T_1 reflections could be indexed in a cubic system, and below T_1 down to 10 K – in an orthorhombic system. The *222* cubic reflection remained unsplit even in the synchrotron XRPD data (Fig. 2a) suggesting no deviations from the orthorhombic structure. Synchrotron XRPD data clearly showed the presence of modulated reflections at RT and at low temperatures (Fig. 2b and 3b), a few weak modulated reflections were also observed in laboratory XRPD data (Fig. S2, ESI†). The temperature dependence of the lattice parameters and unit-cell volume is given in Fig. 4, where the *Immm* model was used in the Rietveld fitting below T_1. Both samples showed the existence of narrow HT regions where the

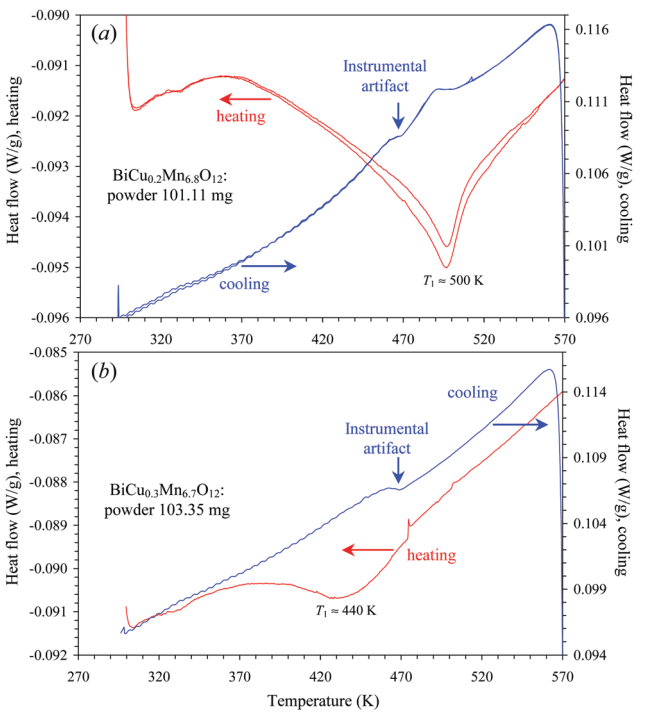

Fig. 1 DSC curves of (a) $BiCu_{0.2}Mn_{6.8}O_{12}$ (two runs) and (b) $BiCu_{0.3}Mn_{6.7}O_{12}$ (one run) on heating (left-hand axes) and cooling (right-hand axes) at 10 K min^{-1}. Note that the heating and cooling difference scale ranges are different. Small bumps near 470 K on cooling curves are instrumental artifacts.

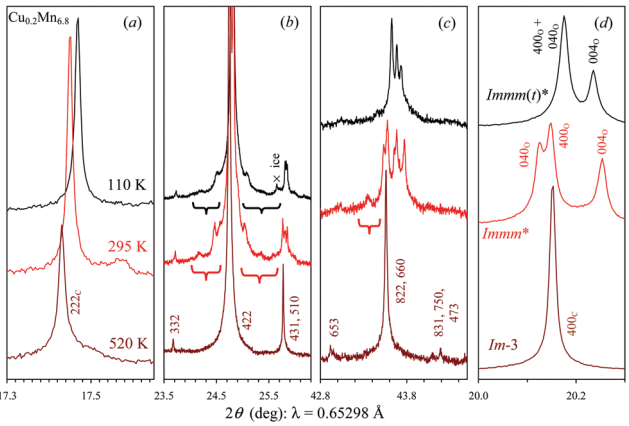

Fig. 2 Fragments of synchrotron XRPD data (BL15XU) of $BiCu_{0.2}Mn_{6.8}O_{12}$ in different 2θ regions at T = 110 K, 295 K and 520 K. Some reflection indexes for the cubic phase (without notations and with the C notation) and the orthorhombic (O) phase are given. A cross marks a possible reflection from ice. Braces show modulated reflections.

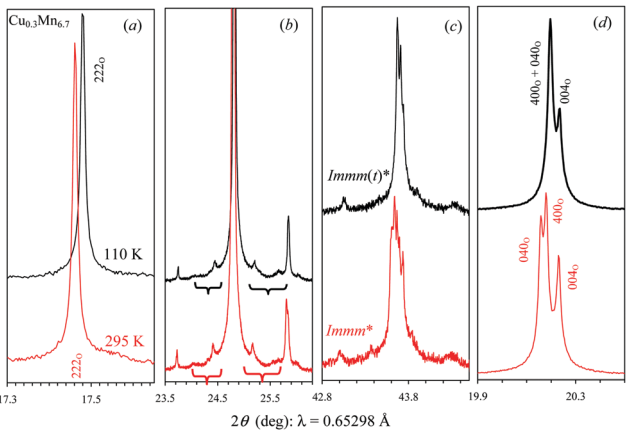

Fig. 3 Fragments of synchrotron XRPD data (BL15XU) of $BiCu_{0.3}Mn_{6.7}O_{12}$ in different 2θ regions at T = 110 K and 295 K. Some reflection indexes for the orthorhombic (O) phase are given. Braces show modulated reflections.

refined orthorhombic (O) lattice parameters a_O and b_O exactly matched indicating that the crystal system became metrically tetragonal. However, there are no tetragonal subgroups of the parent cubic *Im*-3 structure. Therefore, the real symmetry should remain orthorhombic, and we label it HT-*Immm*(t)*, where t stands for pseudo-tetragonal and the asterisk denotes the presence of additional incommensurately modulated reflections. Modulated reflections were observed at all temperatures below T_1 (Fig. S2 and S3, ESI†). There were also LT regions, where the refined lattice parameters a_O and b_O nearly (x = 0.2) or exactly (x = 0.3) matched. The pseudo-tetragonality can also be seen from the merging of the (400) and (040) orthorhombic reflections in the synchrotron XRPD data (Fig. 2d and 3d). Incommensurately modulated reflections remained in the low-temperature *Immm*(t)* phase (LT-*Immm*(t)*, Fig. 2b and 3b), they were only slightly changed compared with the RT data (that is, with the *Immm** phase).

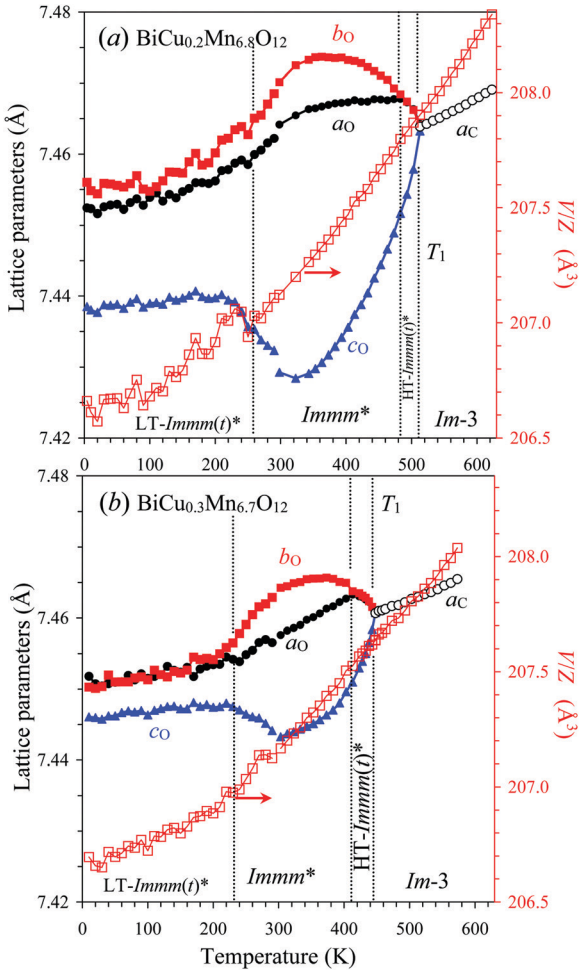

Fig. 4 Temperature dependence of the lattice parameters (left-hand axes) and the unit-cell volume (V/Z) (right-hand axes) in (a) $BiCu_{0.2}Mn_{6.8}O_{12}$ and (b) $BiCu_{0.3}Mn_{6.7}O_{12}$ from laboratory XRPD data. All measurements are performed on heating. C: cubic, O: orthorhombic, t: pseudo-tetragonal. HT: high-temperature, LT: low-temperature. Stars indicate the presence of additional incommensurately modulated reflections. α_V = 1.8(4) × 10^{-5} at 300–610 K for x = 0.2, α_V = 1.5(5) × 10^{-5} at 300–560 K and $\alpha_V \sim 5 \times 10^{-6}$ at 10–210 K for x = 0.3.

Therefore, there are four different crystallographic phases in $BiCu_{0.2}Mn_{6.8}O_{12}$ and $BiCu_{0.3}Mn_{6.7}O_{12}$, *Im*-3 > HT-*Immm*(*t*)* > *Immm** > LT-*Immm*(*t*)*, appearing on cooling.

3.2. $BiCu_xMn_{7-x}O_{12}$ solid solutions with x = 0.4

DSC data of the x = 0.4 sample (Fig. 5a and Fig. S5 of the ESI†) showed the presence of one relatively sharp peak on heating (at $T_1 \approx 360$ K) and cooling and one very broad peak centered at $T_2 \approx 200$ K, which was only observed on heating curves.

Above T_1, all reflections in the synchrotron XRPD data of the x = 0.4 sample can be fitted by the cubic *Im*-3 model, and between T_1 and T_2 in the monoclinic *I*2/*m* model (Fig. S6, ESI†), which was observed in pure $BiMn_7O_{12}$ and slightly doped $BiCu_xMn_{7-x}O_{12}$ with x = 0.1.[20,26] Clear splitting of the *222* cubic reflection was observed below T_1, which then disappeared below T_2. The presence of a single reflection, corresponding

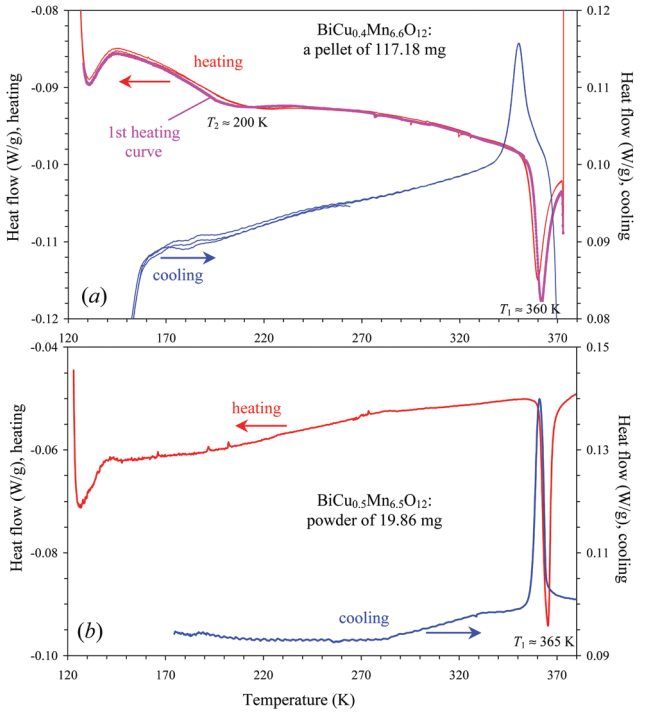

Fig. 5 DSC curves of (a) $BiCu_{0.4}Mn_{6.6}O_{12}$ (three runs) and (b) $BiCu_{0.5}Mn_{6.5}O_{12}$ (one run) on heating (left-hand axes) and cooling (right-hand axes) at 10 K min^{-1}. Note that the heating and cooling difference scale ranges are the same.

to the *222* cubic reflection, confirms that the symmetry is orthorhombic below T_2 (Fig. 6a). However, the *040* and *004* orthorhombic reflections merge at all temperatures below T_2 on synchrotron and laboratory XRPD data. Therefore, lattice parameters below T_2 were refined in space group *Immm* with a constraint, $b_O = c_O$. The temperature dependence of the lattice parameters of $BiCu_{0.4}Mn_{6.6}O_{12}$ is shown in Fig. 7. Therefore, there are three different crystallographic phases in $BiCu_{0.4}Mn_{6.6}O_{12}$, *Im*-3 > *I*2/*m** > *Immm*(*t*)*, appearing on

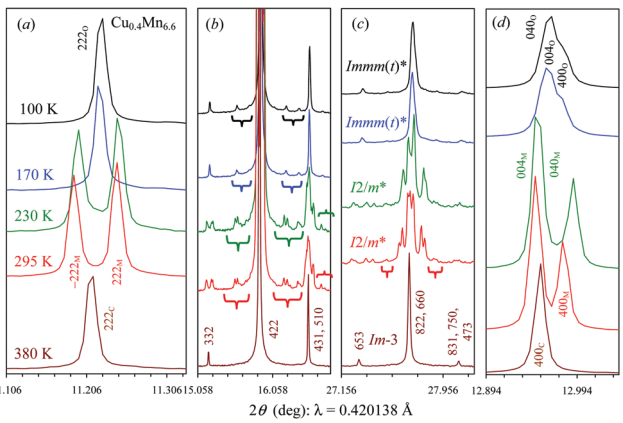

Fig. 6 Fragments of synchrotron XRPD data (BL02B2) of $BiCu_{0.4}Mn_{6.6}O_{12}$ in different 2θ regions at T = 100 K, 170 K, 230 K, 295 K and 380 K. Some reflection indexes for the cubic phase (without notations and with the C notation), the monoclinic (M) phase and the orthorhombic (O) phase are given. Braces show incommensurately modulated reflections.

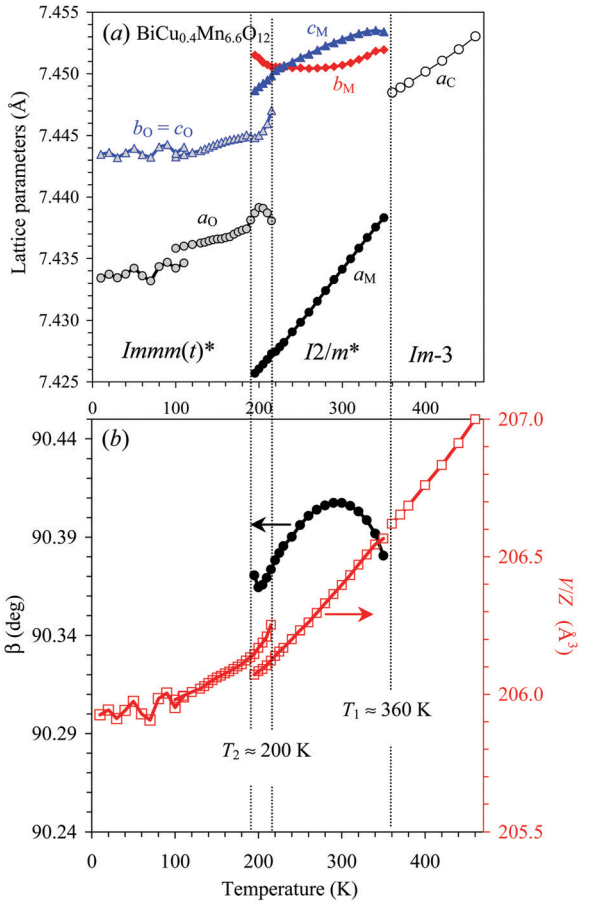

Fig. 7 Temperature dependence of (a) the lattice parameters and (b) monoclinic β angle (left-hand axis) and the unit-cell volume (V/Z) (right-hand axis) in $BiCu_{0.4}Mn_{6.6}O_{12}$ from laboratory XRPD data (from 10 K to 110 K) and synchrotron XRPD data (from 100 K to 460 K). All measurements were performed on heating. M: monoclinic, C: cubic, O: orthorhombic. Stars indicate the presence of additional incommensurately modulated reflections. $\alpha_V = 1.8(2) \times 10^{-5}$ at 360–440 K in the C phase, $\alpha_V = 1.5(3) \times 10^{-5}$ at 195–330 K in the M phase and $\alpha_V = 8.1(1.6) \times 10^{-6}$ at 100–175 K in the O phase (based on synchrotron XRPD data).

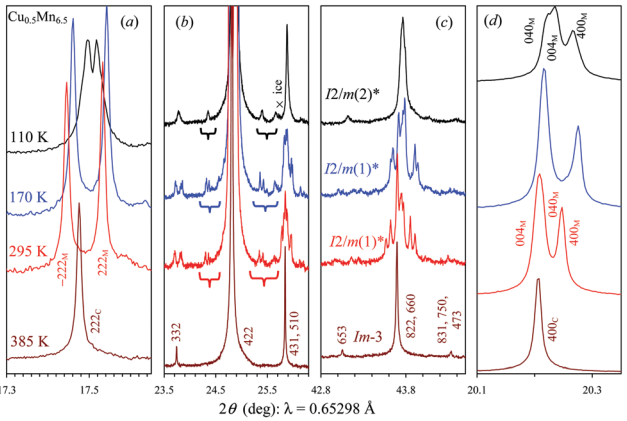

Fig. 8 Fragments of synchrotron XRPD data (BL15XU) of $BiCu_{0.5}Mn_{6.5}O_{12}$ in different 2θ regions at T = 110 K, 170 K, 295 K and 385 K. Some reflection indexes for the cubic phase (without notations and with the C notation) and the monoclinic (M) phase are given. A cross marks a possible reflection from ice. Braces show incommensurately modulated reflections.

cooling, where again the asterisks indicate the presence of additional incommensurate reflections.

3.3. $BiCu_xMn_{7-x}O_{12}$ solid solutions with $x = 0.5$

DSC data of the $x = 0.5$ sample (Fig. 5b) showed the presence of one sharp peak on heating (at $T_1 \approx 365$ K) and cooling. The behavior in $BiCu_{0.5}Mn_{6.5}O_{12}$ below T_1 was similar to that of $BiCu_{0.4}Mn_{6.6}O_{12}$ with one exception in that the monoclinic splitting of reflections (*e.g.*, the *222* cubic reflection) could be observed in laboratory and synchrotron XRPD data at all temperatures below T_1 down to 10 K (Fig. 8 and Fig. S6 of the ESI†). Therefore, the lattice parameters were refined in the space group *I2/m*. Fig. 9 gives the temperature dependence of the lattice parameters of $BiCu_{0.5}Mn_{6.5}O_{12}$ (similar temperature dependence of the lattice parameters was obtained based on neutron diffraction data (Fig. S7, ESI†)); these data show that $BiCu_{0.5}Mn_{6.5}O_{12}$ has the second structural transition near $T_2 \approx 120$ K, where there were steps in the lattice parameters

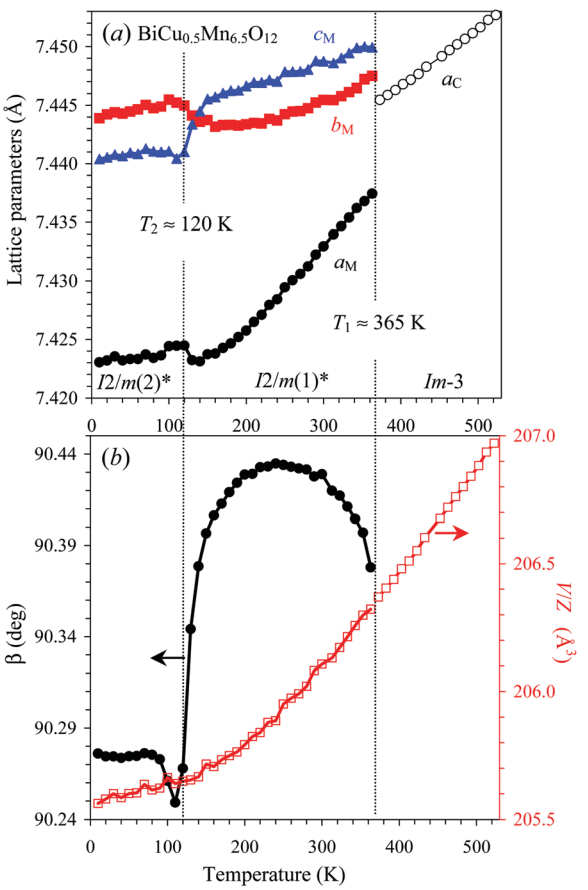

Fig. 9 Temperature dependence of (a) the lattice parameters and (b) monoclinic β angle (left-hand axis) and the unit-cell volume (V/Z) (right-hand axis) in $BiCu_{0.5}Mn_{6.5}O_{12}$ from laboratory XRPD data. Measurements were performed on heating. C: cubic, M: monoclinic. Stars indicate the presence of additional incommensurately modulated reflections. $\alpha_V = 2.0(3) \times 10^{-5}$ at 370–510 K in the C phase and $\alpha_V \sim 5 \times 10^{-6}$ at 10–100 K in the M phase.

and an abrupt change in the behavior of the monoclinic angle. This temperature was below the reach of our DSC experiments; therefore, only one sharp peak was observed in the DSC curves at $T_1 \approx 365$ K (Fig. 5b).

Therefore, there are three different crystallographic phases in $BiCu_{0.5}Mn_{6.5}O_{12}$, *Im*-3 > *I*2/*m*(1)* > *I*2/*m*(2)*, appearing on cooling, where (1) and (2) mean different phases with the same symmetry. The behavior of $BiCu_{0.4}Mn_{6.6}O_{12}$ and $BiCu_{0.5}Mn_{6.5}O_{12}$ is quite similar between T_1 and T_2 including the dome-like changes of the monoclinic angle and the crossing in the temperature dependence of the monoclinic b_M and c_M lattice parameters when approaching T_2. However, below T_2 they adopt different distortions.

The structural evolution of $BiCu_{0.5}Mn_{6.5}O_{12}$ through the phase transitions was studied in detail by neutron diffraction. The most prominent features are presented in Fig. 10. Structural parameters in the average *I*2/*m* and *Im*-3 models at some selected temperatures are summarized in Tables S1 and S2 (ESI†), and Rietveld refinement fits are shown in Fig. S8 (ESI†). As neutron scattering lengths of Cu (7.718 fm) and Mn (−3.73 fm) are very different the Cu/Mn distribution can be precisely studied. Our analysis of the cubic modification (with the minimum number of refined structural parameters) showed that the B sites are solely occupied by Mn. The refined occupation of the A' site (0.149(4)Cu + 0.851Mn) was close to the nominal value (0.167Cu + 0.833Mn). The *Im*-3 > *I*2/*m*(1)* transition is driven by the Jahn–Teller instability of Mn^{3+} cations located at the B sites, and the corresponding orbital order is similar to that observed in the prototype Jahn–Teller perovskite system $LaMnO_3$; the associated structural distortion transforms as the M_2^+ irreducible representation of the parent cubic *Pm*-3*m* space group (for a general ABO_3 perovskite).[35] The amplitude of the M_2^+ distortive mode therefore can be taken as a quantitative measure of the Jahn–Teller distortion averaged over the two symmetry independent B-site Mn cations in the average monoclinic structure of $BiCu_{0.5}Mn_{6.5}O_{12}$. As shown in Fig. 10, at the *I*2/*m*(1)* > *I*2/*m*(2)* transition Jahn–Teller distortions are reduced and at the same time the atomic displacement parameter of the Bi atom is enhanced. The latter most likely indicates an increase in the static off-centric displacements optimizing the lone pair instability. Thus, these experimental findings further support the presence of strong competitions between the lone pair and Jahn–Teller electronic instabilities. Apparently, the LT (iso)structural transitions in other compositions of the series with $x = 0.2$, 0.3 and 0.4 are similar in origin, although additional studies and quantitative characterizations of the structural modulations are required to confirm this assumption.

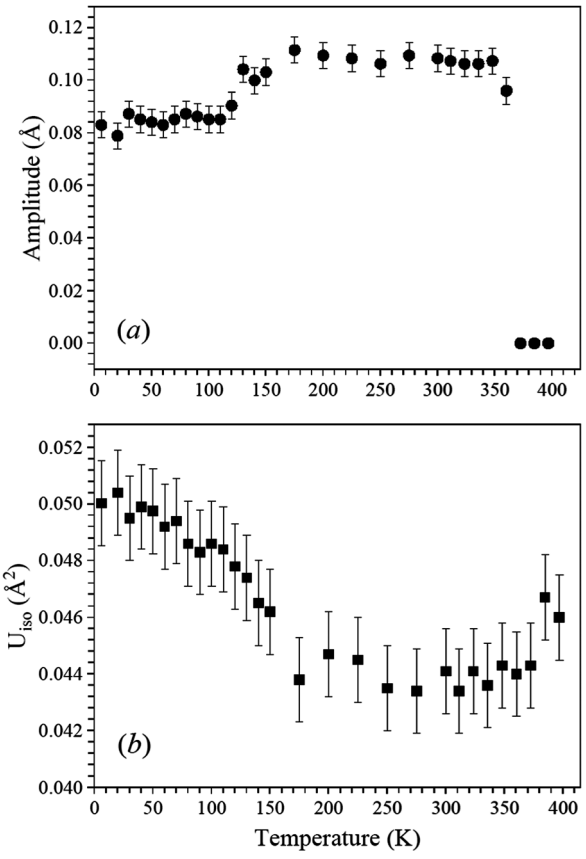

Fig. 10 Temperature dependence of (a) the average amplitude of the Jahn–Teller distortions for two octahedral sites (Mn4 and Mn5) and (b) the atomic displacement parameter of the Bi site in the ideal (0, 0, 0) positions in $BiCu_{0.5}Mn_{6.5}O_{12}$ from neutron diffraction data.

3.4. $BiCu_xMn_{7-x}O_{12}$ solid solutions with $x = 0.6$ and 0.7

DSC data (Fig. 11) showed the presence of two relatively sharp peaks on heating with $T_1 \approx 330$ K ($x = 0.6$), $T_1 \approx 289$ K ($x = 0.7$), $T_2 \approx 206$ K ($x = 0.6$) and $T_2 \approx 206$ K ($x = 0.7$). Cooling curves revealed large hysteresis at T_2; the hysteresis reached about 25 K for $x = 0.7$ (as a peak was centered near 181 K on cooling). The hysteresis was probably larger for $x = 0.6$; this is why no clear peaks were observed on cooling as the peak may have been hidden by extrinsic effects (below about 160–170 K the DSC system could not support a constant cooling rate of 10 K min^{-1} resulting in peak-like artifacts).

Above T_1 and below T_2, reflections on laboratory and synchrotron XRPD data could be indexed in the cubic space group *Im*-3, and between T_1 and T_2 – in the monoclinic space group *I*2/*m* (Fig. 12 and Fig. S9 of the ESI†). The temperature dependence of the lattice parameters and unit-cell volume is given in Fig. 13. The monoclinic angle β (Fig. 13b) shows a dome-like feature in both compounds, but this feature was less pronounced in comparison with the dome-like feature of $BiCu_{0.5}Mn_{6.5}O_{12}$ in the *I*2/*m*(1)* phase (Fig. 9b). It is also interesting that the monoclinic b_M and c_M lattice parameters were the same in $BiCu_{0.6}Mn_{6.4}O_{12}$ in the whole temperature range where this phase is stable. Therefore, both $BiCu_{0.6}Mn_{6.4}O_{12}$ and $BiCu_{0.7}Mn_{6.3}O_{12}$ show a re-entrant phase transition to the cubic phase and the following sequence of phase transformations, *Im*-3 > *I*2/*m** > *Im*-3. Note that the *I*2/*m** phases should actually be slightly different in both compounds as they have different incommensurately modulated reflections (Fig. 12).

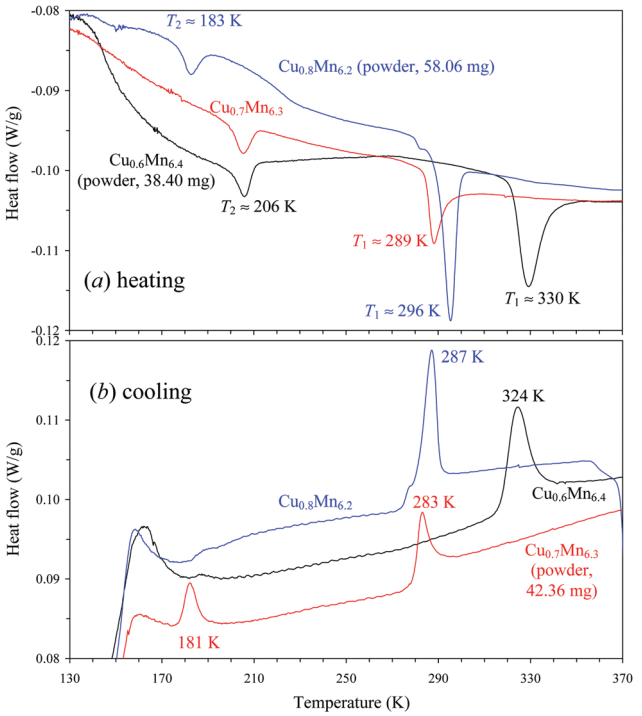

Fig. 11 DSC curves of $BiCu_{0.6}Mn_{6.4}O_{12}$ (black), $BiCu_{0.7}Mn_{6.3}O_{12}$ (red), and $BiCu_{0.8}Mn_{6.2}O_{12}$ (blue) on (a) heating and (b) cooling at 10 K min^{-1}. Note the heating and cooling difference scale ranges are the same.

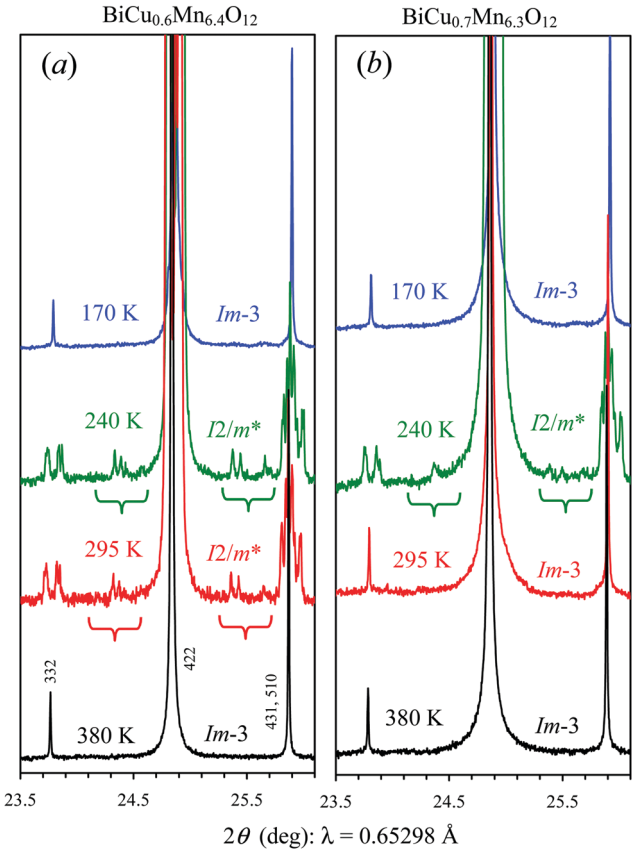

Fig. 12 Fragments of synchrotron XRPD data (BL15XU) of (a) $BiCu_{0.6}Mn_{6.4}O_{12}$ and (b) $BiCu_{0.7}Mn_{6.3}O_{12}$ in a 2θ region of 23.5–26.1 deg at T = 170 K, 240 K, 295 K and 380 K. Some reflection indexes for the cubic phase (without notations) are given. Braces show modulated reflections.

3.5. $BiCu_xMn_{7-x}O_{12}$ solid solutions with $x = 0.8$

DSC data (Fig. 11) showed the presence of two relatively sharp peaks on heating with $T_1 \approx 296$ K and $T_2 \approx 183$ K. Cooling curves revealed only one peak centered at 287 K, the second peak could not be seen due to extrinsic effects on DSC cooling curves.

Laboratory and synchrotron XRPD data revealed the following sequence of phase transitions on cooling: *Im*-3 > *R*-3 > *I*2/*m* > *Im*-3 (Fig. 14 and Fig. S10 of the ESI†). However, the *R*-3 phase was not observed as purely single-phase on synchrotron XRPD data: at 290 K, about 35 wt% of the cubic *Im*-3 phase remained, and about 15 wt% of the monoclinic *I*2/*m* phase already appeared at 275 K. A smaller measurement step would probably be needed to detect a single *R*-3 phase. The *R*-3 and *I*2/*m* phases coexisted from 275 K down to 223 K. The single *I*2/*m* phase was only observed at 206 K. Because of the complex phase co-existence, the temperature dependence of the lattice parameters was extracted from synchrotron XRPD data between 120 and 300 K; below 160 K, where the cubic phase is stable, laboratory XRPD data were used (Fig. 15). It should be noted that no modulated reflections were observed in this monoclinic *I*2/*m* phase. Also, no modulated reflections were found in the *R*-3 phase.

3.6. Composition–temperature phase diagram of $BiCu_xMn_{7-x}O_{12}$

A complete composition–temperature phase diagram of the $BiCu_xMn_{7-x}O_{12}$ system (Fig. 16) can be constructed based on the results of this work for x = 0.2–0.8 and the literature data for x = 0,[20] 0.05, 0.1,[26] 0.9, 1.0, 1.1 and 1.2.[27] We emphasize that available laboratory and synchrotron XRPD data do not allow us to distinguish between centrosymmetric and non-centrosymmetric space groups at the moment. Therefore, we always assigned centrosymmetric space groups. Detailed structural analysis or other methods will be needed in future studies to determine the presence or absence of a center of symmetry. For example, a polar space group of $R3(00\gamma)t$ was found in $BiCu_{0.1}Mn_{6.9}O_{12}$ below about 400 K based on the crystal structure analysis of neutron diffraction data and the observation of a ferroelectric *P*–*E* hysteresis loop.[26] Very detailed structural studies will also be needed in the future to determine full structural models, which could account for all observed modulated reflections. The construction of such models is out of the scope of the present study.

Here we mention that for both monoclinic and orthorhombic structures there are several non-equivalent non-centrosymmetric structures. For instance, in the case of the *Immm* space group, there are four non-centrosymmetric isotropy subgroups with the same reflection conditions as *Immm*, namely *I*222, *I*2*mm*, *Im*2*m* and *Imm*2. In spite of the fact that the latter three are *Imm*2 in the standard setting, the corresponding structures are non-equivalent and imply different directions to

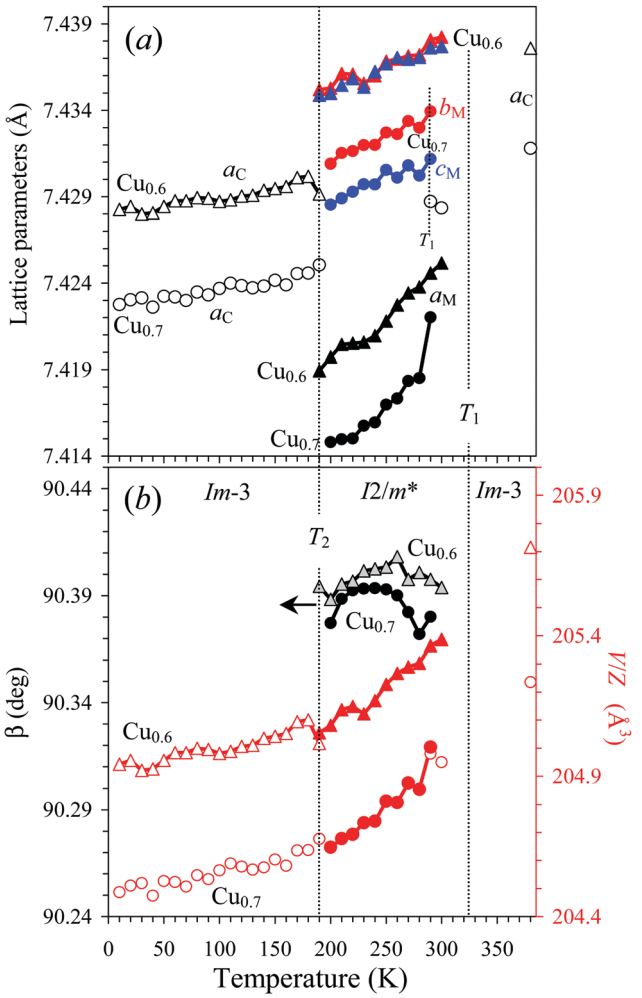

Fig. 13 Temperature dependence of (a) the lattice parameters and (b) monoclinic β angle (left-hand axis) and the unit-cell volume (V/Z) (right-hand axis) in $BiCu_{0.6}Mn_{6.4}O_{12}$ (triangles) and $BiCu_{0.7}Mn_{6.3}O_{12}$ (circles) from laboratory XRPD data (below 300 K). Synchrotron XRPD data were used above 300 K. C: cubic, M: monoclinic. Stars indicate the presence of additional modulated reflections. $\alpha_V \sim 4 \times 10^{-6}$ at 10–180 K in the C phase for x = 0.6 and 0.7.

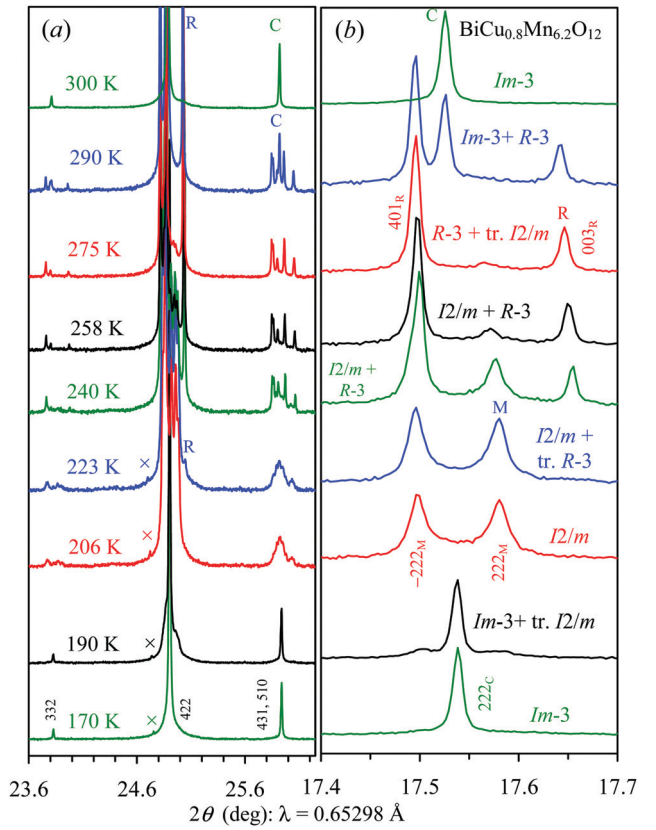

Fig. 14 Fragments of synchrotron XRPD data (BL15XU) of $BiCu_{0.8}Mn_{6.2}O_{12}$ in different 2θ regions at different temperatures. Some reflection indexes for the cubic phase (without notations and with the C notation), the monoclinic (M) phase, and the R-3 phase (R) are given. Crosses mark a reflection from ice. tr.: trace.

become polar. The $I2/m$ space group has Im and $I2$ non-centrosymmetric isotropy subgroups.

At high temperatures, the parent cubic Im-3 structure is stable for all the compositions. On cooling, the cubic structure transforms into different modifications driven by the orbital ordering of Mn^{3+} cations (as in the $I2/m$ phases) and/or charge ordering of Mn^{3+}/Mn^{4+} cations (realized, for example, in the R-3 phase for x = 0.8–1.1), where Mn^{4+} cations appear as a result of Cu^{2+} doping. Neutron diffraction demonstrated that Cu^{2+} cations are localized in the square-planar A' site as expected because Cu^{2+} cations strongly prefer Jahn–Teller-distorted sites. As Mn^{4+} cations cannot be located in square-planar sites they should exclusively appear at the octahedral B sites.

The first HT structural transition from the cubic phase (at T_1) appears to be first-order for x = 0–0.1 and 0.4–1.1 judging from sharp peaks on DSC curves, hysteresis between the heating/cooling DSC curves and abrupt changes of the lattice parameters. However, no detectable jumps of the (normalized) unit-cell volume were observed, for example, for x = 0.4 (Fig. 7) and 0.5 (Fig. 9). On the other hand, the first HT transition showed all signs of a second-order phase transition for x = 0.2 and 0.3, where the HT-$Immm(t)$* phase first emerges from the cubic phase. Namely, the orthorhombic lattice parameters merged gradually (Fig. 4), no detectable jumps of the (normalized) unit-cell volume were observed, and there were very broad DSC anomalies (Fig. 1). However, any transition from the cubic Im-3 to either $Immm$, $I2/m$ or R-3 must be first order based on the symmetry grounds. It is related to the fact that the relevant irreducible representations, mediating the corresponding symmetry lowering, allow a third power invariant in the Landau free-energy decomposition. So, all these representations do not satisfy the Landau criteria for continuous phase transitions. LT structural phase transitions for x = 0.4–1.1 are characterized by large DSC hysteresis for all compositions (if observable), abrupt changes of the lattice parameters and jumps on the (normalized) unit-cell volume suggesting their strong first-order nature.

During the first HT structural transition large structural distortions are realized. However, at lower temperatures, structural distortions are suppressed for x = 0.2–0.5 as can be seen from the reduced reflection splitting, the merging of some

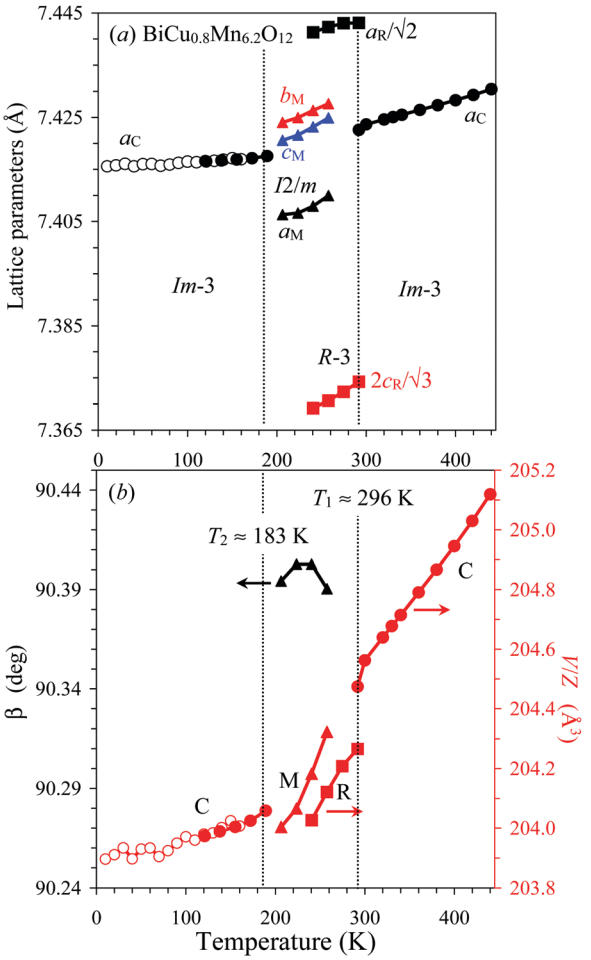

Fig. 15 Temperature dependence of (a) the lattice parameters and (b) monoclinic β angle (left-hand axis) and the unit-cell volume (V/Z) (right-hand axis) in $BiCu_{0.8}Mn_{6.2}O_{12}$ from laboratory XRPD data (open circles; 10–160 K) and synchrotron XRPD data (filled symbols; 120–440 K). All measurements were performed on heating. C: cubic, M: monoclinic. R: R-3. $\alpha_V = 1.93(13) \times 10^{-5}$ in the HT C phase, $\alpha_V = 2.3(6) \times 10^{-5}$ in the R phase, $\alpha_V = 3(1) \times 10^{-5}$ in the M phase and $\alpha_V = 6(3) \times 10^{-6}$ at 120–180 K in the LT C phase.

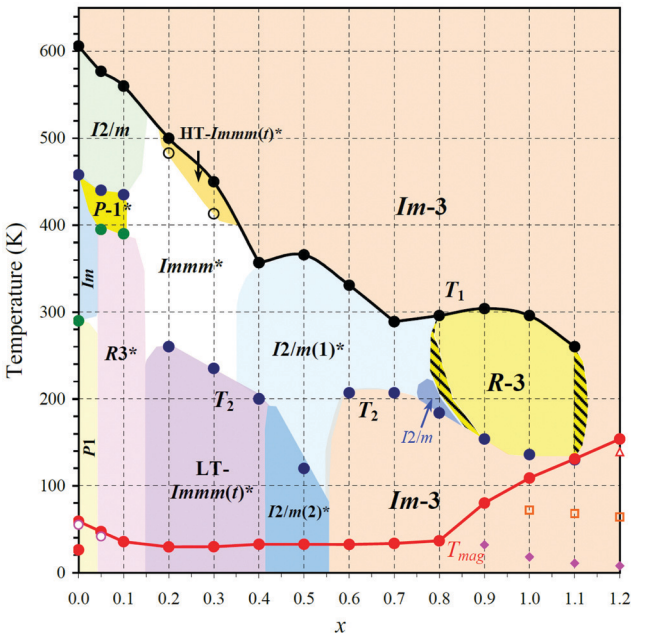

Fig. 16 Composition–temperature phase diagram of $BiCu_xMn_{7-x}O_{12}$ solid solutions for $0 \leq x \leq 1.2$. Stars indicate the presence of additional incommensurately modulated reflections, t stands for pseudo-tetragonal. Shaded regions show mixed-phase regions. Magnetic transition temperatures (T_{mag}: red and pink symbols) are also plotted for completeness (but detailed magnetic studies will be reported elsewhere). T_1 denotes a phase transition from the high-temperature cubic Im-3 phase. T_2 denotes the lowest temperature structural phase transition.

lattice parameters, and temperature evolution of the Jahn–Teller distortions (Fig. 10a). For the x = 0.6–1.1 compositions, structural distortions are completely suppressed with the re-entrance of the cubic phase. There are no (static) polar, orbital and charge orderings in the cubic phase. Therefore, the re-entrance of the cubic phase suggests that competition among different instabilities in $BiCu_xMn_{7-x}O_{12}$ is very strong and of comparable strength and intensifies with decreasing temperature, and the system is frustrated to a degree when it cannot choose a preferable instability. We note that the re-entrant low-temperature cubic phases demonstrate nearly zero thermal expansion with the volumetric coefficient of thermal expansion ($\alpha_V = (1/V)^*\Delta V/\Delta T$) of about 4×10^{-6}.

The $BiCu_{0.8}Mn_{6.2}O_{12}$ composition is located between two major structural distortions, $I2/m$ and R-3. This fact could be the origin of its complex behavior. The R-3 phase is characterized by B-site Mn^{3+}/Mn^{4+} charge ordering (where the ideal 3 : 1 ratio of $Mn^{3+}:Mn^{4+}$ is realized in $BiCuMn_6O_{12}$).[27] As the $Mn^{3+}:Mn^{4+}$ ratio at the B sites approaches the ideal value in $BiCu_{0.8}Mn_{6.2}O_{12}$ the charge-ordered distortion first wins. But the R-3 phase has unusual compressed Mn^{3+} octahedra, and such Jahn–Teller distortions are very unstable.[36] Therefore, the $I2/m$ phase wins on further cooling as it has usual elongated Jahn–Teller distortions. Polar instabilities from the presence of Bi^{3+} cations could add additional frustration to the system eventually leading to the cubic symmetry on further cooling. We note that even small compositional inhomogeneity could complicate the behavior of $BiCu_{0.8}Mn_{6.2}O_{12}$ even though we did not observe any evidence of inhomogeneity in the cubic modifications (such as, reflection broadening or splitting).

The behavior of the x = 0.6–1.1 compositions can also be discussed from the opposite direction, that is, during heating. Different ordered states, such as spin-, charge-, orbital-ordered, and superconducting states, are destroyed when temperature increases in the vast majority of condensed-matter systems. A famous exception to this general rule is the so-called Pomeranchuk effect, when the liquid ground state of ^{3}He transforms to a solid when temperature increases.[37,38] The $BiCu_xMn_{7-x}O_{12}$ solid solutions with x = 0.6–1.1 can also be considered as exceptions to the general rule as their disordered cubic ground states transform to the orbital-ordered state (x = 0.6 and 0.7) or the orbital- and charge-ordered states (x = 0.8–1.1) when temperature increases.

4. Conclusion

Undoped $BiMn_7O_{12}$ has active electronic instabilities related to Bi^{3+} lone-pair electrons and Jahn–Teller Mn^{3+} cations. Both instabilities are in play resulting in the orbital order transition, $Im\text{-}3 > I2/m$, and in polar distortions, $I2/m > Im > P1$. Carrier doping by Cu^{2+} was found to tune the competing electronic instabilities of $BiMn_7O_{12}$ resulting in a complex composition–temperature phase diagram of the $BiCu_xMn_{7-x}O_{12}$ solid solution, with the appearance of a number of different crystallographic phases the majority of which hosted additional incommensurate structural modulations. Competition between instabilities in $BiCu_xMn_{7-x}O_{12}$ intensifies for $x = 0.6$–1.1 resulting in the re-entrance of the high-temperature cubic phase in the ground state. The re-entrant cubic phases have nearly zero thermal expansion.

Author contributions

Alexei A. Belik: conceptualization, investigation, formal analysis, data curation, writing – original draft, writing – review and editing. Yoshitaka Matsushita: investigation. Masahiko Tanaka: investigation. Roger D. Johnson: formal analysis, investigation, writing – review & editing. Dmitry D. Khalyavin: formal analysis, investigation, writing – review and editing.

Conflicts of interest

The authors declare no competing financial interest.

Acknowledgements

This work was partly supported by JSPS KAKENHI Grant Numbers JP19H05819 and JP20H05276, a research grant (40–37) from Nippon Sheet Glass Foundation for Materials Science and Engineering, and Innovative Science and Technology Initiative for Security (Grant Number JPJ004596) from Acquisition, Technology, and Logistics Agency (ATLA), Japan. The synchrotron radiation experiments were performed at SPring-8 with the approval of the NIMS Synchrotron X-ray Station (Proposal Numbers: 2016B4504, 2017A4503 and 2019A4501) and Japan Synchrotron Radiation Research Institute (JASRI) (Proposal No. 2021A1334). We thank Dr Y. Katsuya for his assistance at BL15XU of SPring-8, and Dr S. Kobayashi for his assistance at BL02B2 of SPring-8. RDJ acknowledges support from a Royal Society University Research Fellowship.

References

1 J.-S. Zhou and J. B. Goodenough, Unusual evolution of the magnetic interactions versus structural distortions in $RMnO_3$ perovskites, *Phys. Rev. Lett.*, 2006, **96**, 247202.
2 L. Zhang, A. Dönni, V. Y. Pomjakushin, K. Yamaura and A. A. Belik, Crystal and magnetic structures and properties of $(Lu_{1-x}Mn_x)MnO_3$ solid solutions, *Inorg. Chem.*, 2018, **57**, 14073–14085.
3 L. Zhang, Y. Matsushita, K. Yamaura and A. A. Belik, Five-fold ordering in high-pressure perovskites RMn_3O_6 (R = Gd–Tm and Y), *Inorg. Chem.*, 2017, **56**, 5210–5218.
4 A. N. Vasil'ev and O. S. Volkova, New functional materials $AC_3B_4O_{12}$ (Review), *Low Temp. Phys.*, 2007, **33**, 895–914.
5 B. Bochu, J. Chenavas, J. C. Joubert and M. Marezio, High pressure synthesis and crystal structure of a new series of perovskite-like compounds CMn_7O_{12} (C = Na, Ca, Cd, Sr, La, Nd), *J. Solid State Chem.*, 1974, **11**, 88–93.
6 A. Prodi, E. Gilioli, R. Cabassi, F. Bolzoni, F. Licci, Q. Huang, J. W. Lynn, M. Affronte, A. Gauzzi and M. Marezio, Magnetic Structure of the high-density single-valent e_g Jahn-Teller system $LaMn_7O_{12}$, *Phys. Rev. B: Condens. Matter Mater. Phys.*, 2009, **79**, 085105.
7 H. Okamoto, M. Karppinen, H. Yamauchi and H. Fjellvag, High-temperature synchrotron X-ray diffraction study of $LaMn_7O_{12}$, *Solid State Sci.*, 2009, **11**, 1211–1215.
8 R. Cabassi, F. Bolzoni, E. Gilioli, F. Bissoli, A. Prodi and A. Gauzzi, Jahn-Teller-induced crossover of the paramagnetic response in the singly valent eg system $LaMn_7O_{12}$, *Phys. Rev. B: Condens. Matter Mater. Phys.*, 2010, **81**, 214412.
9 F. Mezzadri, M. Calicchio, E. Gilioli, R. Cabassi, F. Bolzoni, G. Calestani and F. Bissoli, High-pressure synthesis and characterization of $PrMn_7O_{12}$ polymorphs, *Phys. Rev. B: Condens. Matter Mater. Phys.*, 2009, **79**, 014420.
10 M. Verseils, F. Mezzadri, D. Delmonte, B. Baptiste, Y. Klein, S. Shcheka, L. C. Chapon, T. Hansen, E. Gilioli and A. Gauzzi, Effect of chemical pressure induced by La^{3+}/Y^{3+} substitution on the magnetic ordering of $(AMn_3)Mn_4O_{12}$ quadruple perovskites, *Phys. Rev. Mater.*, 2017, **1**, 064407.
11 N. Imamura, M. Karppinen, T. Motohashi, D. Fu, M. Itoh and H. Yamauchi, Positive and negative magnetodielectric effects in A-site ordered $(BiMn_3)Mn_4O_{12}$ perovskite, *J. Am. Chem. Soc.*, 2008, **130**, 14948–14949.
12 F. Mezzadri, G. Calestani, M. Calicchio, E. Gilioli, F. Bolzoni, R. Cabassi, M. Marezio and A. Migliori, Synthesis and characterization of multiferroic $BiMn_7O_{12}$, *Phys. Rev. B: Condens. Matter Mater. Phys.*, 2009, **79**, 100106(R).
13 W. A. Slawinski, H. Okamoto and H. Fjellvag, Triclinic crystal structure distortion of multiferroic $BiMn_7O_{12}$, *Acta Crystallogr., Sect. B: Struct. Sci., Cryst. Eng. Mater.*, 2017, **73**, 313–320.
14 N. Imamura, M. Karppinen and H. Yamauchi, Synthesis and properties of monoclinic and cubic forms of the A-site-ordered $(BiMn_3)Mn_4O_{12}$ perovskite, *Chem. Mater.*, 2009, **21**, 2179–2183.
15 H. Okamoto, N. Imamura, M. Karppinen, H. Yamauchi and H. Fjellvag, Square coordinated MnO_2-units in $BiMn_7O_{12}$, *Inorg. Chem.*, 2010, **49**, 8709–8712.
16 H. Okamoto, N. Imamura, M. Karppinen, H. Yamauchi and H. Fjellvag, Crystal structure of the monoclinic and cubic polymorphs of $BiMn_7O_{12}$, *J. Solid State Chem.*, 2010, **183**, 186–191.
17 F. Mezzadri, M. Buzzi, C. Pernechele, G. Calestani, M. Solzi, A. Migliori and E. Gilioli, Polymorphism and multiferroicity in $Bi_{1-x/3}(Mn^{III}{}_3)(Mn^{III}{}_{4-x}Mn^{IV}{}_x)O_{12}$, *Chem. Mater.*, 2011, **23**, 3628–3635.

18 N. Imamura, K. Singh, D. Pelloquin, C. Simon, T. Sasagawa, M. Karppinen, H. Yamauchi and A. Maignan, Magnetodielectric response of square-coordinated MnO_2 unit in cubic $BiMn_7O_{12}$, *Appl. Phys. Lett.*, 2011, **98**, 072903.

19 A. Gauzzi, G. Rousse, F. Mezzadri, G. L. Calestani, G. Andre, F. Bouree, M. Calicchio, E. Gilioli, R. Cabassi, F. Bolzoni, A. Prodi, P. Bordet and M. Marezio, Magnetoelectric coupling driven by inverse magnetostriction in multiferroic $BiMn_3Mn_4O_{12}$, *J. Appl. Phys.*, 2013, **113**, 043920.

20 A. A. Belik, Y. Matsushita, Y. Kumagai, Y. Katsuya, M. Tanaka, S. Y. Stefanovich, B. I. Lazoryak, F. Oba and K. Yamaura, Complex structural behavior of $BiMn_7O_{12}$ quadruple perovskite, *Inorg. Chem.*, 2017, **56**, 12272–12281.

21 L. Zhang, N. Terada, R. D. Johnson, D. D. Khalyavin, P. Manuel, Y. Katsuya, M. Tanaka, Y. Matsushita, K. Yamaura and A. A. Belik, High-pressure synthesis, structures, and properties of trivalent A-site-ordered quadruple perovskites RMn_7O_{12} (R = Sm, Eu, Gd, and Tb), *Inorg. Chem.*, 2018, **57**, 5987–5998.

22 T. Kimura, T. Goto, H. Shintani, K. Ishizaka, T. Arima and Y. Tokura, Magnetic control of ferroelectric polarization, *Nature*, 2003, **426**, 55–58.

23 I. Yamada, Novel catalytic properties of quadruple perovskites, *Sci. Technol. Adv. Mater.*, 2017, **18**, 541–548.

24 A. A. Belik, S. Iikubo, T. Yokosawa, K. Kodama, N. Igawa, S. Shamoto, M. Azuma, M. Takano, K. Kimoto, Y. Matsui and E. Takayama-Muromachi, Origin of the monoclinic-to-monoclinic phase transition and evidence for the centrosymmetric crystal structure of $BiMnO_3$, *J. Am. Chem. Soc.*, 2007, **129**, 971–977.

25 P. Baettig, R. Seshadri and N. A. Spaldin, Anti-polarity in ideal $BiMnO_3$, *J. Am. Chem. Soc.*, 2007, **129**, 9854–9855.

26 D. D. Khalyavin, R. D. Johnson, F. Orlandi, P. G. Radaelli, P. Manuel and A. A. Belik, Emergent helical texture of electric dipoles, *Science*, 2020, **369**, 680–684.

27 A. A. Belik, Y. Matsushita and D. D. Khalyavin, Reentrant structural transitions and collapse of charge and orbital orders in quadruple perovskites, *Angew. Chem., Int. Ed.*, 2017, **56**, 10423–10427.

28 Y. S. Glazkova, N. Terada, Y. Matsushita, Y. Katsuya, M. Tanaka, A. V. Sobolev, I. A. Presniakov and A. A. Belik, High-pressure synthesis, crystal structures, and properties of $CdMn_7O_{12}$ and $SrMn_7O_{12}$ perovskites, *Inorg. Chem.*, 2015, **54**, 9081–9091.

29 F. Izumi and T. Ikeda, A Rietveld-analysis program RIETAN-98 and its applications to zeolites, *Mater. Sci. Forum*, 2000, **321-324**, 198–205.

30 M. Tanaka, Y. Katsuya and A. Yamamoto, A new large radius imaging plate camera for high-resolution and high-throughput synchrotron X-ray powder diffraction by multi-exposure method, *Rev. Sci. Instrum.*, 2008, **79**, 075106.

31 M. Tanaka, Y. Katsuya, Y. Matsushita and O. Sakata, Development of a synchrotron powder diffractometer with a one-dimensional X-ray detector for analysis of advanced materials, *J. Ceram. Soc. Jpn.*, 2013, **121**, 287–290.

32 S. Kawaguchi, M. Takemoto, K. Osaka, E. Nishibori, C. Moriyoshi, Y. Kubota, Y. Kuroiwa and K. Sugimoto, High-throughput powder diffraction measurement system consisting of multiple MYTHEN detectors at beamline BL02B2 of SPring-8, *Rev. Sci. Instrum.*, 2017, **88**, 085111.

33 L. C. Chapon, P. Manuel, P. G. Radaelli, C. Benson, L. Perrott, S. Ansell, N. J. Rhodes, D. Raspino, D. Duxbury, E. Spill and J. Norris, Wish: the new powder and single crystal magnetic diffractometer on the second target station, *Neutron News*, 2011, **22**, 22–25.

34 C. J. Rodriguez, Recent advances in magnetic structure determination by neutron powder diffraction, *Phys. B*, 1993, **193**, 55–69.

35 M. A. Carpenter and C. J. Howard, Symmetry rules and strain/order-parameter relationships for coupling between octahedral tilting and cooperative Jahn-Teller transitions in ABX_3 perovskites. I. Theory, *Acta Crystallogr., Sect. B: Struct. Sci., Cryst. Eng. Mater.*, 2009, **65**, 134–146.

36 S. V. Streltsov and D. I. Khomskii, Jahn-Teller distortion and charge, orbital, and magnetic order in $NaMn_7O_{12}$, *Phys. Rev. B: Condens. Matter Mater. Phys.*, 2014, **89**, 201115.

37 I. Pomeranchuk, On the theory of liquid ^{3}He, *Zh. Eksp. Teor. Fiz.*, 1950, **20**, 919–926.

38 Y. Saito, F. Y. Yang, J. Y. Ge, X. X. Liu, T. Taniguchi, K. Watanabe, J. I. A. Li, E. Berg and A. F. Young, Isospin Pomeranchuk effect in twisted bilayer graphene, *Nature*, 2021, **592**, 220–224.

